Auto-Processing of Filtered Rayleigh Scattering Images Including Mie and Background Scattering Contributions

Sean W. Powers[1,*], Evan P. Warner[1], Gwibo Byun[1], K. Todd Lowe[1]

1: Kevin T. Crofton Dept. of Aerospace and Ocean Engineering, Virginia Tech, Blacksburg VA, USA

*Corresponding author: kelowe@vt.edu

Keywords: Filtered Rayleigh Scattering, Velocimetry, Auto-Processing, Scattering, and Planar Measurements

ABSTRACT

Filtered Rayleigh scattering (FRS) is a non-intrusive, optical-based technique that allows for simultaneous, measurements of three-component velocity, static temperature, and static pressure. The experimental results of this paper will be time-averaged due to long exposure times. The method of post-processing the raw images to get these variables is a non-trivial task. The post-processing scheme starts with building a model to generate simulated spectra given inputs of velocity, temperature, and pressure values which can be iterated upon to match the experimental spectrum. The model also includes Mie scattering and background scattering contributions that must be taken into account. This process can be lengthy and so it is important to make spectrum generation/iteration as fast as possible. This is done through the use of support vector spectrum approximation (SVSA), which is a machine learning algorithm, as well as a multivariable minimum error solver based on the least-squares fit between the simulated data and the experimental data. To prove the methodology, simulated results were first compared at different signal-to-noise ratios to determine the expected uncertainty at each signal-to-noise ratio (SNR) level. It was shown that to achieve an error of less than 1% in all variables (velocity, static temperature, Mie intensity ratio, and background intensity ratio), the SNR must be near 40dB. This kind of SNR level is generally not expected in an experiment. Therefore, a representative experiment was conducted which included Mie and background scattering contributions. It was shown that manually processed data was capable of achieving velocity results that were within 2% of the probe data. No other variables were solved for manually. The auto-processing scheme was able to achieve an error of approximately 2.5% in velocity when compared to probe data. It was also capable of providing static temperature, Mie intensity ratio, and background intensity ratio values. The manual iteration results took several days to achieve while the auto-processing took about an hour. This methodology is capable of automatically processing images from experiments with Mie and background scattering contributions while saving time.

1. Introduction

The post-processing of filtered Rayleigh scattering (FRS) data for non-intrusive measurements of 3-component velocity, static temperature, static pressure, background scattering, and Mie scattering is a non-trivial task. With the ever-increasing interest in non-intrusive measurements, it is

clear that a fast and robust method for evaluating the raw data is needed. The ability of FRS to measure vector and scalar quantities without particles introduced into the flow sets it apart from well-known techniques such as particle image velocimetry (PIV) and Doppler global velocimetry (DGV), all of which require particles. The algorithm developed in this work is capable of automatically processing images from experiments with Mie and background scattering contributions. This algorithm is applied towards FRS in which clear examples are given both in simulation as well as experimentation.

Rayleigh scattering is a wave optics phenomenon resulting from the interaction of light and matter on the scale of, or smaller than, the wavelength of the laser light. The ability to not need particles in the flow is attractive for measurement conditions where it would be hard or impossible to seed. Add in the ability to take planar measurements of scalar and vector quantities simultaneously and Rayleigh scattering becomes extremely attractive. Summarizing the key attributes of the Rayleigh scattering signal,

1. The Rayleigh scattering resulting from the interaction between light and matter is elastic, meaning there is no energy transfer between them.
2. Rayleigh scattering occurs down to molecular levels.
3. The probability of photons scattering from a gas molecule (scattering intensity) increases with the amount of matter in the volume and the scattering cross-section of the gas (static density/pressure).
4. Light scattered off matter in motion is Doppler shifted in frequency proportional to its bulk velocity (Velocity).
5. In a stagnant gas, individual molecules are always in motion, (kinetic theory of gases) imparting a Doppler shift proportional to the speed of the individual molecules (Static Temperature).

Items three through five yield the measurement principles, namely that direct measurements of static pressure (3) and static temperature (4) can be used to get static density from the state equation, while the mean Doppler shifted signal yields flow velocity. These effects are all observed through the use of a molecular absorption filter, in this case, an iodine vapor cell is used. A typical setup will be shown later.

2. Filtered Rayleigh scattering theoretical modeling

The current Virginia Tech-developed processing code determines the static temperature and velocity values by using a least-squares fit. The least-squares fit compares the measured scattering spectrum to a theoretical spectral model. The theoretical model comes from the convolution of

the Rayleigh scattering spectral model with a theoretical transmission spectral model for an iodine vapor cell in the vicinity of 532nm light. This specific wavelength is typical for frequency doubled, diode pumped lasers using gain media such as Nd:YVO_4 or Nd:YAG lasers. Doll et al. (2014, 2017, 2018) use similar techniques. The addition of Mie and background scattering into the theoretical model has been covered extensively by Boyda et al. (2018a,b, 2019) and Saltzman et al. (2019). However, the user must manually iterate to get the theoretical spectrum to match the measured spectrum. This is laborsome and often results in slightly different outcomes for different users due to the least-squares minimization falling into different local minima in the solution space. Therefore, an automatic, iteratively solved scheme has been developed. This method will be covered in detail in this section.

The model must first start by generating the theoretical Rayleigh scattering signal. This can be done using the numerical Tenti S6 model (Tenti et al. (1974); Pan et al. (2004); McManus et al. (2019); Pan (2003)). This model has been accepted as the current best approximation and is a slight correction to the original Hanson-Morse model (Hanson & Morse (1967); Hanson et al. (1969)). This correction was needed due to an approximation that was made and subsequently proven incorrect by Tenti et al. (1974). The Tenti S6 model is a set of six linear equations that are solved simultaneously to form the Rayleigh scattering line shape given dimensionless input parameters x, y, internal heat capacity (c_{int}), internal relaxation number (R_{int}), and Euken factor (f_u) (much simpler than previous models, yet still complex). y, R_{int}, and f_u are dependent on static flow properties and their relationship can be seen below (Pan et al. (2004)).

$$y = \frac{p}{\eta k v_0} = \frac{n_0 k_b T}{\eta k v_0} \tag{1}$$

$$R_{int} = \frac{3\eta_b}{2\eta} \frac{(3/2 + c_{int})}{c_{int}} \tag{2}$$

$$f_u = \frac{m\sigma}{\eta k_b (3/2 + c_{int})} \tag{3}$$

where n_0 is the number density (amount of molecules in a given volume), k_b is the Boltzmann constant, η is the dynamic viscosity, k is the wave vector magnitude defined as $k = 4\pi \sin(\theta/2)/\lambda$ with θ being the scattering angle and λ the wavelength of the incident light, v_0 is the most probable gas kinetic velocity defined as $v_0 = \sqrt{2k_b T/m}$ with m being the molecular mass of the gas, η_b is the bulk viscosity, and σ is the thermal conductivity. The reader is encouraged to refer to Tenti et al. (1974); Pan et al. (2004); McManus et al. (2019); Pan (2003) for a more in-depth discussion and derivation behind this model line shape.

A nominal flow case was chosen to investigate the effects of the number of nodes versus generation time where a wavenumber of zero is the laser frequency. Nodes represent the number of points to include in the generation of the line shape. The model will have to iteratively generate a large

number of these spectra for each pixel. Therefore, it is of the utmost importance that this run as fast as possible. Ten-thousand nodes were used as the "true" case and then compared. Five hundred nodes were decided to be used in the model due to its low error and fast computation time relative to the "true" case (Fig. 1).

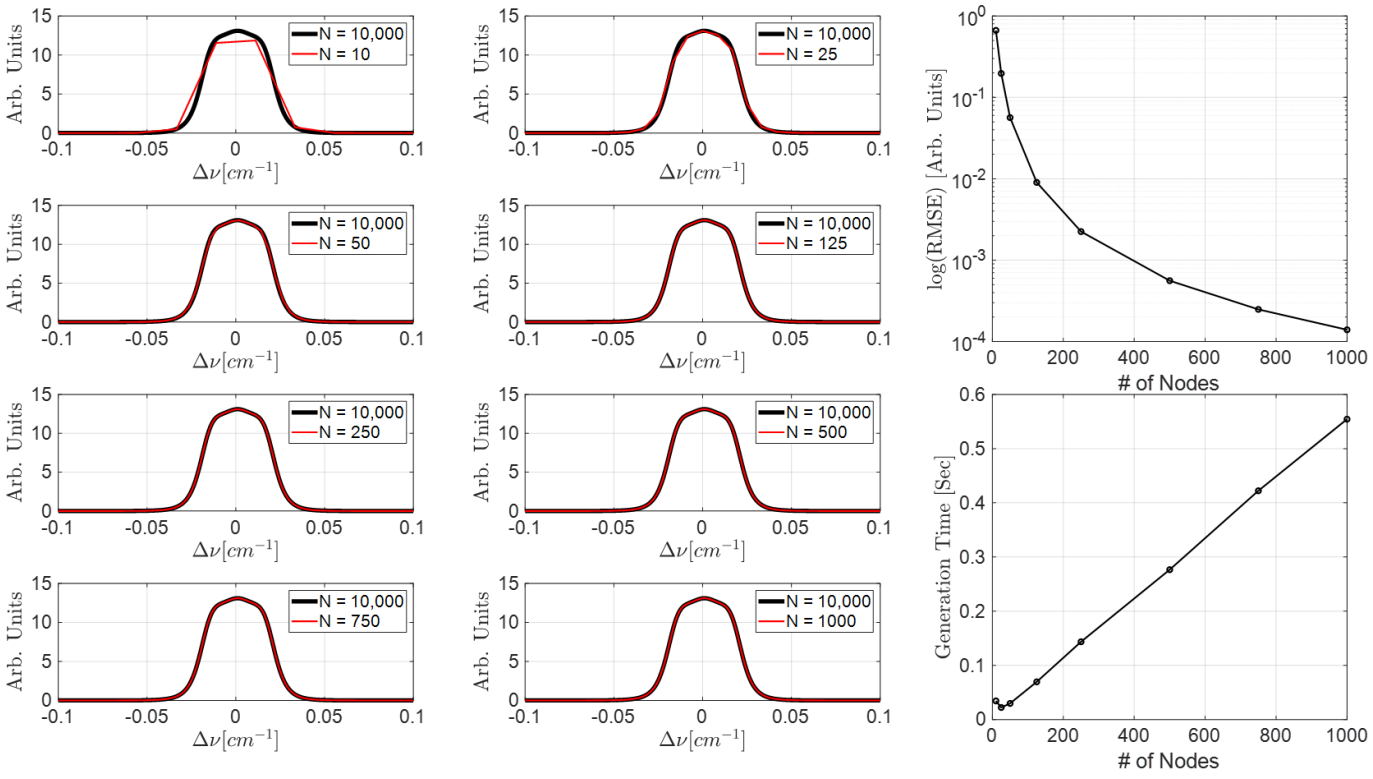

Figure 1. Tenti S6 model results using a different number of nodes. RMSE and generation time are also included.

The Tenti S6 model has been looked at specifically for FRS purposes by McManus et al. (2019). Specifically, McManus investigated the Tenti S6 model for combustion-relevant gases using an experimental setup. This was done by comparing the measured FRS signals to the simulated FRS signals that were generated by combining the Tenti S6 model and an experimentally verified iodine absorption model. It was experimentally shown that over a temperature range of 300K to 2400K, with representative exhaust gases from a combustion cycle, the Tenti S6 model was sufficiently accurate (less than 4% average difference).

Alternative numerical models were pursued such as a newer, simpler, Rayleigh scattering line shape model that was introduced by Witschas (2011). This model is an easily processable, analytical alternative to the highly complex Tenti S6 model. However, the author does acknowledge that the Tenti S6 model is still the best. In limited applications, the Witschas model can be faster and with an error smaller than 0.85%. The application is limited to a defined range for the ratio of the acoustic wavelength to the mean free path between collisions, 0 and 1.027. Such a model may be useful if processing time or computation power is limited. It was decided that this model did not offer enough advantages over the original Tenti S6 model given the incurred errors.

Finally, Hunt et al. (2020) asserts that the Tenti S6 model can be computationally expensive, especially when using it in an iterative scheme. Again, an iterative scheme is being used to match simulated FRS data to experimental FRS data. This assertion is not unlike that made by Witschas. Instead of an analytical model like Witschas, Hunt opts for a machine learning approach. This method is called the support vector spectrum approximation (SVSA). This uses vector regression and singular value decomposition to create an efficient, accurate, and well-conditioned approximation of any existing spectral line shape.

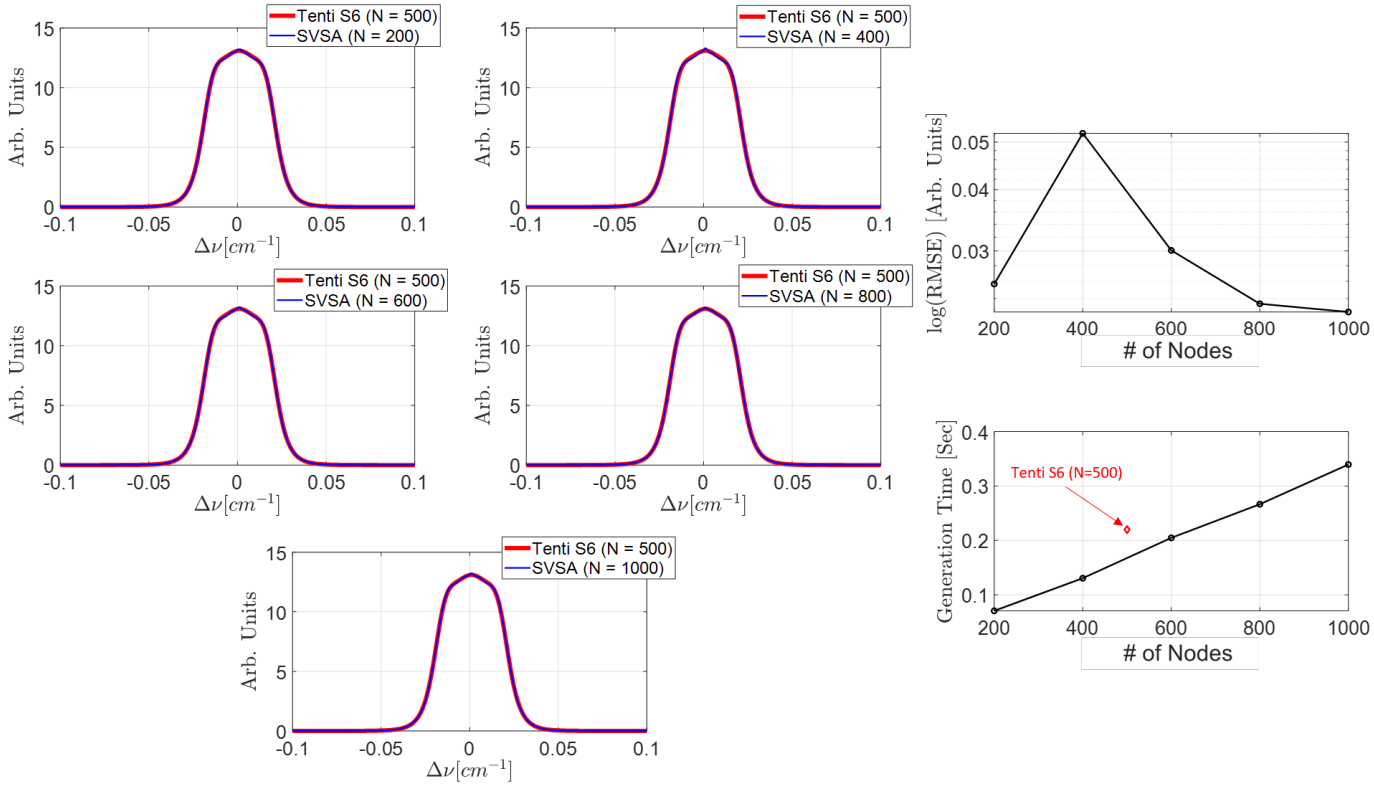

Figure 2. Support vector spectrum approximation (SVSA) comparison to Tenti S6 model with a different number of nodes. RMSE and generation time are also included.

The SVSA results seen in Fig. 2 are compared against the chosen Tenti S6 model with five-hundred nodal points. It should be mentioned that this implementation of SVSA was trained using the Tenti S6 model. It is possible to use the SVSA method to decrease the nodal points even further which drives down the computation time without significantly increasing error. These results show that error does not go down much as a result of increasing the number of SVSA nodal points. However, the computation time increases significantly. Generally, the authors have used at most 180 individual wavenumbers in an experiment. To keep the number of nodal points above that number, two-hundred nodal points are used with the SVSA method. In an experiment, the data will not be taken exactly at the nodal wavenumbers. Therefore, the simulated Rayleigh scattering spectrum needs to be interpolated to match the wavenumbers used in the experiment. Using more nodal points than experimental wavenumbers allows the interpolation error to stay low. In prac-

tice, the authors have noted that the SVSA method is approximately four times as fast compared to the original Tenti S6 model with less than 1% error (see Fig. 2). Specifically, this method was developed to optimize the design of an FRS experiment of a complex flow. It is important to note that the SVSA approximation results in a slight deviation near the peak of the Rayleigh scattering spectrum (can be seen if closely examining Fig. 2). This is shown to be negligible as the deviation in peak behavior is essentially "filtered out" during the convolution operation with the theoretical iodine transmission spectrum (discussed later).

Now that the Rayleigh scattering spectrum has been generated, the Rayleigh scattering spectrum line shape can be shown to have a dependence on temperature, pressure, and scattering angle (Fig. 3). The scattering angle is defined by the angle between the laser propagation vector ($\hat{i}$) and the observation vector ($\hat{o}$). Figure 3A shows the temperature dependence which largely results in the Rayleigh line shape being broadened as the full width at half maximum (FWHM) increases proportionally to $\sqrt{T}$ (Boguszko & Elliott (2005)). Figure 3B shows the pressure dependence which only alters the shape near the peak. The scattering angle has the largest change on the Rayleigh scattering line shape, where large variations in shape and intensity can be seen (Fig. 3C). Back-scattering ($\theta < 90°$) results in a much stronger (higher intensity) Rayleigh scattering signal. Finally, Fig. 3D shows a typical experimental setup with the required vector definitions. All Rayleigh scattering line shapes shown thus far have been normalized by Eq. (4) such that Eq. (5) is satisfied (integral intensity is unity). This will be important when accounting for Mie and background scattering contributions.

$$S_{Ray_{Norm}} = \frac{S_{Ray}}{\int_{-\infty}^{\infty} S_{Ray} d\nu} \tag{4}$$

$$\int_{-\infty}^{\infty} S_{Ray_{Norm}} d\nu = 1 \tag{5}$$

Not included in Fig. 3 are the effects of velocity. The bulk velocity of the flow will Doppler shift the entire Rayleigh scattering spectrum to the left or right on the wavenumber spectrum depending on the sign of the velocity measured. This velocity can be computed using the Doppler shift equation (Eq. (6)) as long as the laser propagation and observation vector are known as described on the right side of Fig. 3. Note that the velocity is sensed in the direction of the difference between the scattered light direction and the laser propagation direction. All velocity results in this paper will be this in terms of this sensed velocity. In an experiment, these would have to be rotated back to orthogonal coordinates.

$$\Delta\nu_D = \frac{(\hat{o} - \hat{i}) \cdot \overrightarrow{V}}{\lambda} \tag{6}$$

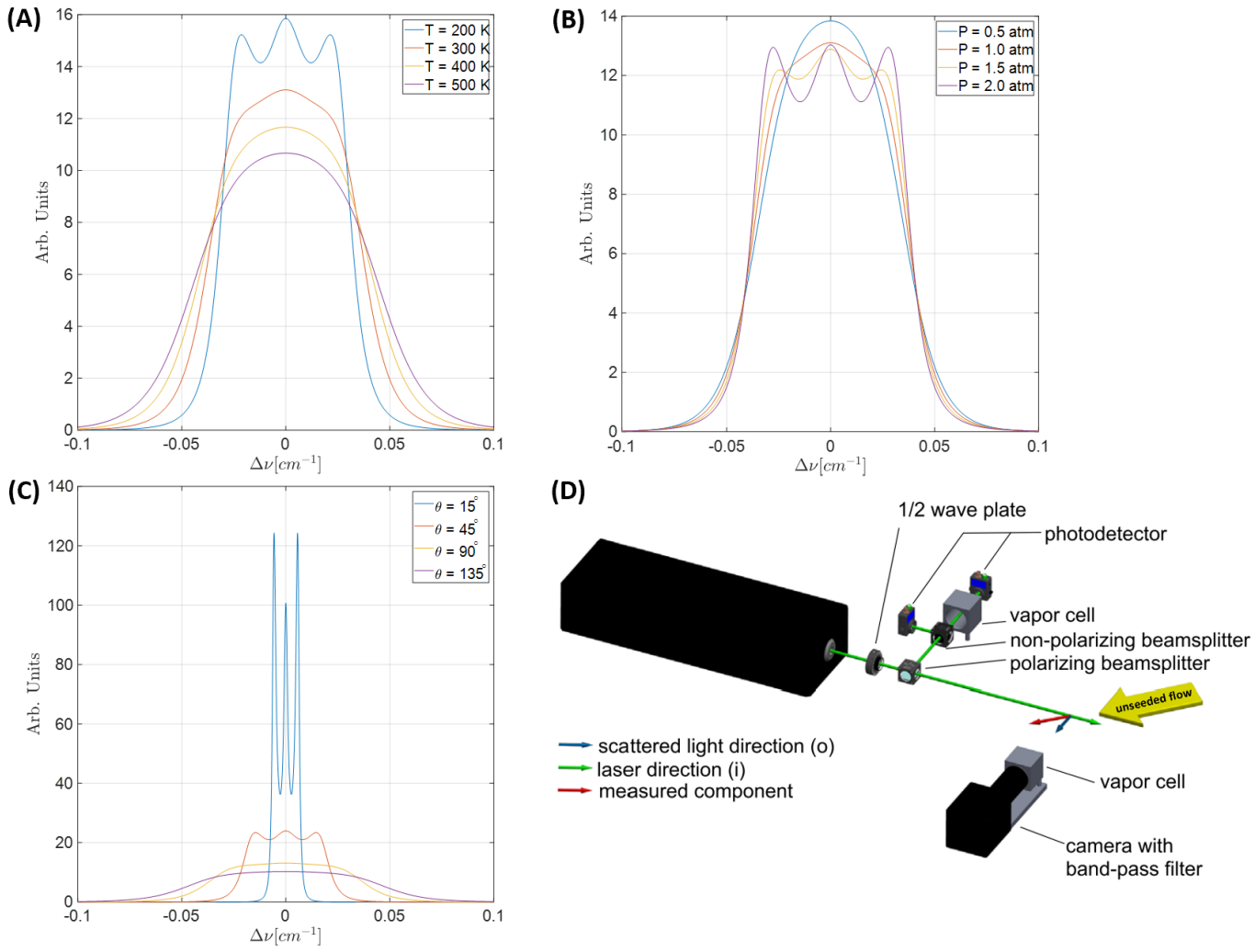

Figure 3. Rayleigh line shape dependencies and vector definitions. (A) Temperature variation with pressure held at 1 atm and scattering angle held constant at 90 degrees. (B) Pressure variation with temperature held at 300K and scattering angle held at 90 degrees. (c) Scattering angle variation with temperature held at 300K and pressure at 1 atm. (D) Simplified diagram of FRS measurement with vector definitions of interest (adapted from Cadel & Lowe (2015)).

Next, Mie scattering must be accounted for. Mie scattering is the scattering of the incident light (laser light) off of particles in the air that are of the same size or larger than that of the wavelength of light. Since the Mie scattering is due to particles moving with the flow, the scattered light will Doppler shift along with the rest of the Rayleigh scattering spectrum. For the present work, the authors have defined the width of the Mie scattering spectrum using 200 MHz corresponding to 5 - 18% turbulence intensity of the flow - representative of flow cases generated from Virginia Tech facilities (Boyda et al. (2019)). One-half of this width becomes the standard deviation input to the normal probability density function used to produce the Mie scattering spectrum. This spectrum can be seen in Fig. 4A.

Now, background scattering must be accounted for. Background scattering can also be called geometric scattering as it is the scattering of the incident light (laser light) off of objects that can be

seen with the camera. This scattering will not be Doppler shifted with the flow since the background is (generally) not moving. This can be seen in Fig. 4B as the resulting intensity increase is offset from the Doppler-shifted frequency (located at the nominal center frequency of the laser). The background spectrum is also generated using a normal probability density function; however, the mean is placed at the offset wavenumber and the standard deviation is defined by the laser frequency variation. The current work makes use of a Coherent Verdi-V18 laser with a stated laser frequency stability of 5 MHz. Compared to Mie scattering, background scattering is much narrower, but the resulting intensity peak is much greater in magnitude.

Finally, all three scattering contributions can be added together to give the total scattering spectrum which can be seen in Fig. 4C. This figure clearly shows that when a bulk velocity is applied to the flow, background and Mie scattering will have different effects on the final spectrum. Just like with Rayleigh scattering, the Mie and background scattering equations need to be normalized (Eqs. 7 and 8). The only difference is that the normalized spectrum is multiplied by an integral intensity ratio. Later, the iterative code will iterate on these intensity ratios to back out Mie and background scattering levels. Finally, the three spectra can be combined via Eq. (9) to find the conglomerate spectrum.

$$S_{Mie_{Norm}} = \frac{S_{Mie}}{\int_{-\infty}^{\infty} S_{Mie} d\nu} * IR_{Mie} \qquad \text{where,} \qquad IR_{Mie} = \frac{I_{Mie}}{I_{Rayleigh}} = \frac{\int_{-\infty}^{\infty} S_{Mie} d\nu}{\int_{-\infty}^{\infty} S_{Rayleigh} d\nu} \tag{7}$$

$$S_{Bknd_{Norm}} = \frac{S_{Bknd}}{\int_{-\infty}^{\infty} S_{Bknd} d\nu} * IR_{Bknd} \qquad \text{where,} \qquad IR_{Bknd} = \frac{I_{Background}}{I_{Rayleigh}} = \frac{\int_{-\infty}^{\infty} S_{Bknd} d\nu}{\int_{-\infty}^{\infty} S_{Rayleigh} d\nu} \tag{8}$$

$$S_{Tot_{Norm}} = S_{Mie_{Norm}} + S_{Bknd_{Norm}} + S_{Ray_{Norm}} \tag{9}$$

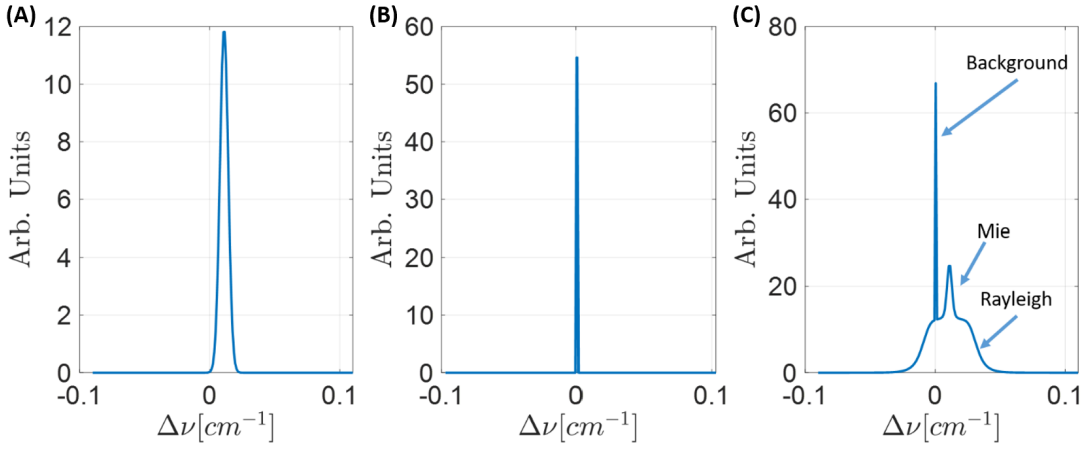

Figure 4. Combination of Mie and background scattering to make the final Rayleigh signal. (A) Mie scattering. (B) Background scattering. (C) Total combined scattering spectrum. Generation parameters: Temperature of 300K, pressure of 1 atm, Mie and background scattering intensity ratios of 0.1, and velocity of 300 m/s.

A molecular vapor filter can be used with known absorption levels to attenuate the scattering signals and leave behind just the Rayleigh scattering signal. This is the difference between pure Rayleigh scattering and filtered Rayleigh scattering. An iodine vapor cell works very well with 532nm (green) laser light (Shimizu et al. (1983)) due to several deep transitions that occur in the spectral region around this wavelength. The specific iodine transmission spectrum model used in the current work with the 532nm laser is the same as developed by Forkey and colleagues (Forkey et al. (1997, 1996)). However, alternative combinations of laser light and molecular filters do exist such as Mercury at 253.77nm (Yalin & Miles (1999)), Cesium at 389, 852, and 894nm (Fischer et al. (2008)), and Barium at 355nm (Hetlage et al. (2019)).

The iodine absorption spectrum for a vapor cell at a pressure of 2 torr and a length of 127 mm can be seen in Fig. 5 for a wide range of wavenumbers. The red box outlines the wavenumber range to which the experimental results will use. This box has been zoomed in to show the sharp features that will be used to attenuate the total Rayleigh scattering signal. Finally, the total Rayleigh scattering signal has been plotted on top of the iodine absorption spectrum. Note that the Mie and background scattering contributions rise above a normalized intensity of one. Leveraging the sharp absorption features of iodine, one aims to filter out these undesirable contributions as much as possible.

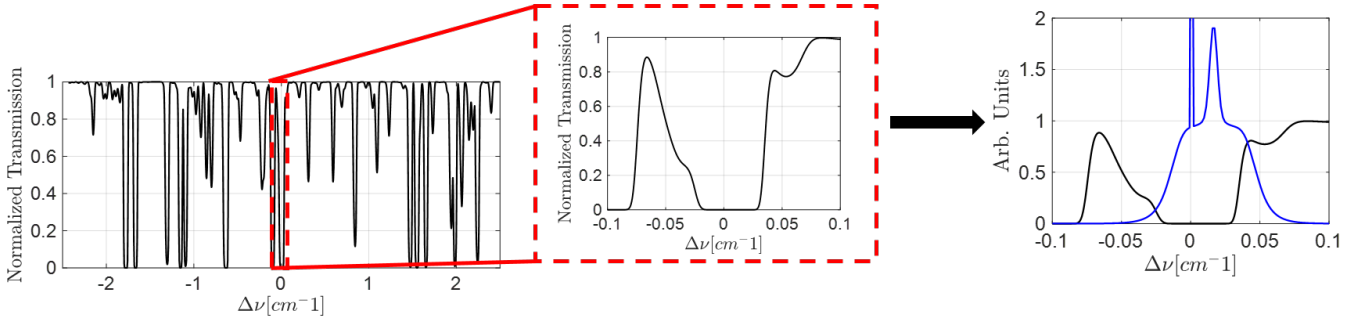

Figure 5. Iodine transmission spectrum (Forkey spectrum) for a vapor cell with pressure of 2 torr and a length of 127 mm. Rayleigh scattering signal also included.

Boyda et al. (2020) describes that the actual signal received by the measurement device (camera) is the convolution of the transmission spectrum of the molecular filter and the Rayleigh, Mie, and background (geometric) scattering spectrum. This can be seen in Eq. (10) where the transmission spectrum of the iodine cell is defined by T_{iodine}.

$$S_S(v) = S_{Tot} \otimes T_{iodine} = \int_{-\infty}^{\infty} S_{Tot}(\eta) T_{iodine}(\nu - \eta) d\eta \tag{10}$$

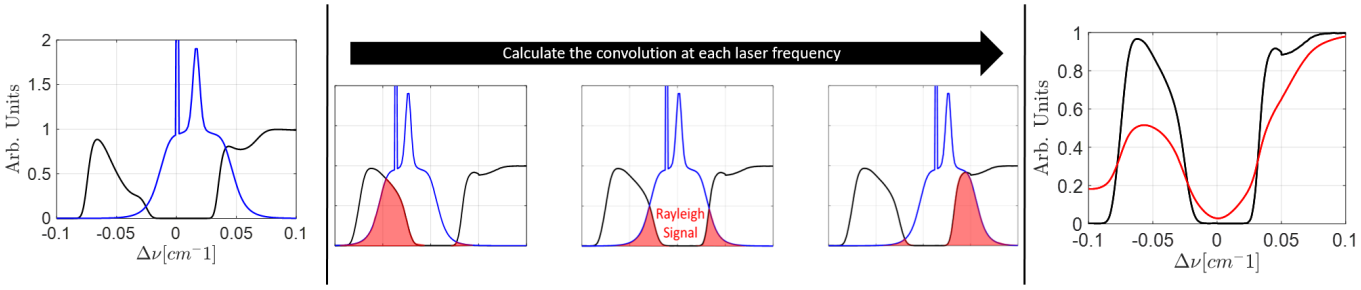

Figure 6. Calculating the convoluted signal. Left: Total scattering signal and Forkey spectrum. Middle: Remaining Rayleigh scattering signal is in red after being filtered. Right: Final convolved spectrum in red plotted with the Forkey spectrum in black.

Since the laser is scanned over a wavenumber range, a Rayleigh scattering signal is produced at each wavenumber. This wavenumber corresponds to a specific absorptivity level in the iodine transmission spectrum. Therefore, the convolution must be calculated at each wavenumber and then reconstructed to form the final convoluted spectrum. Figure 6 shows this process as the far left side shows the Forkey spectrum in black and the Rayleigh spectrum in blue on the center laser frequency. The middle part of this figure shows the remaining FRS signal in red as a majority of the Rayleigh scattering signal is filtered out. The shape of this shaded region contains information about the velocity, temperature, background, and Mie scattering of the flow. Finally, on the far right side, the original absorptivity spectrum is shown in black with the constructed convolved signal shown in red. Notice the clear differences between the two. This red line is what can be compared to the experimental data as the camera looks through an iodine cell. In other words, the camera is measuring the convolved spectrum, not the pure Rayleigh signal.

Now that the method to get the convoluted spectra has been defined, the results from Fig. 3 can be repeated. Except this time, it will be done with the convoluted spectrum instead of the pure Rayleigh scattering signal. The results of this convolution can be seen in Fig. 7. As the temperature rises, the troughs become lower and the peaks become higher. The apparent change due to pressure cannot be seen easily but has a similar effect as temperature. The scattering angle variation has a major impact on the spectra shape, as expected. In the backward scattering regime, the Doppler broadening effect becomes less prominent as scattering angle approaches 0°, yielding less Rayleigh scattered light (Fig. 3C). This decrease in sensed Rayleigh scattered light results in the convoluted spectrum to appear more and more like the iodine absorption spectrum. Finally, velocity variations behave exactly as expected. No change is seen in the spectrum shape; however, the entire spectrum has been shifted due to the Doppler effect.

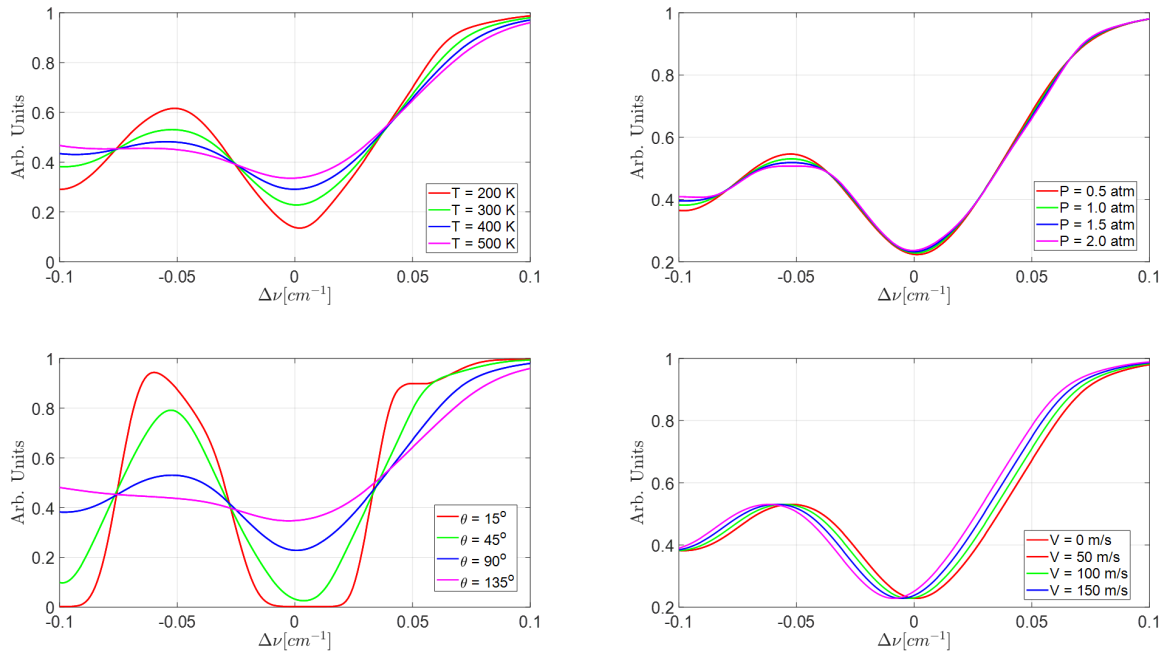

Figure 7. Convolution spectra dependencies on flow properties. Top left: Temperature variation with pressure held at 1 atm, theta at 90 degrees, and velocity at 0 m/s. Top right: Pressure variation with the temperature at 300K, theta at 90 degrees, and velocity at 0 m/s. Bottom left: Angle variation with the temperature at 300K, pressure at 1 atm, and velocity at 0 m/s. Bottom right: Velocity variation with the temperature at 300K, pressure at 1 atm, and theta at 90 degrees.

Additionally, the effects of Mie and background scattering can be investigated on the convoluted spectrum. The results of this study can be seen in Fig. 8. The top-left chart examines the differences in Mie intensity ratios as defined by Eq. (7). Outside of the low transmission region, Mie scattering greatly increases the convoluted intensity. The top-right chart examines the differences in different background scattering ratios as defined by Eq. (8). Outside of the low transmission region, background scattering has a very similar effect as Mie scattering. However, this effect has been offset due to the bulk velocity of the flow (100 m/s in this example). The differences between these two scattering contributions can be seen in the bottom right chart where the solid lines are for Mie scattering only, and the dashed lines are for background scattering only. The effect of each causes a slightly different spectrum shape. This is important because it will be shown that the iterative solver scheme can pick out the differences between the two. Finally, in the bottom right, the combination spectra including both Mie and background scattering contributions are shown.

An important feature to note is that of the "normal range" in Fig. 8. This is the range in which normal FRS measurements are focused due to the very low impact of Mie and background scattering (shape of the curve changes very little). However, this area is limited in the number of points available to match the experimental data. It has been shown that this limited data region immediately impacts the expected uncertainty by Boyda et al. (2019). In contrast, this method attempts to use the entire available spectrum while accounting for the Mie and background scattering to greatly increase the number of data points available.

Traditionally, predicting Mie and background scattering values requires some sort of knowledge from the experimental setup or can be found via manual iteration to match the simulated spectrum to the experimental spectrum. Either way, this process is inaccurate and prolongs the processing time required. These costs are what motivated the development of an automatic processing scheme in which the unique spectrum generated for one pixel during an experiment is processed through an automatic process that iteratively varies variables like velocity, temperature, Mie scattering, and background scattering values until the simulated spectrum best matches the experimental spectrum. At present, variables like random noise and shot noise are not accounted but are part of future work. The automatic processing scheme will be defined in detail in the next section.

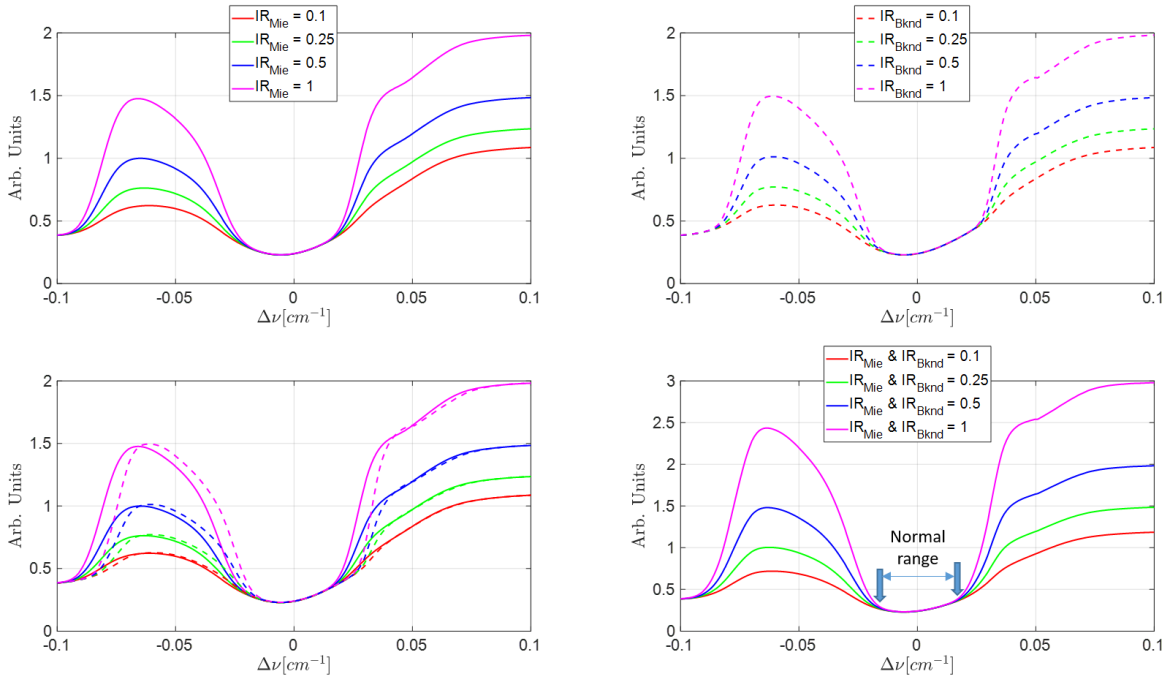

Figure 8. Convolution spectra dependencies on Mie and background scattering. Top left: Mie variation with a velocity of 0 m/s and 0 background scattering. Top right: Background scattering with a velocity of 100 m/s and 0 Mie scattering. Bottom left: Top two charts plotted on top of one another. Note the difference between the Mie scattering contribution and background scattering contribution. Bottom right: Combined Mie and background scattering contributions.

3. Automatic Processing and Uncertainty Results

Automatic processing, in this case, refers to an iteratively solved minimum error for an unconstrained multivariable function using the derivative free-method (fminsearch in MATLAB (Lagarias et al. (1998))). The objective function to be minimized is defined by the least-squares error between the experimental data (measured) and the simulated data (Eq. (11)). The simulated data is generated using the derived model shown in the previous section. To minimize Eq. (11), static temperature, velocity, Mie intensity ratio, and background intensity ratio are all iterated upon. To make sure these values remain physical and within the scope of the model, a lower bound was

placed on each variable. For example, the Tenti S6 model does not allow for temperatures less than 200 K. Physically, it is also known that the intensity ratios for Mie and background scattering cannot be below zero. These are the only physical variable constraints placed on the solver. The only other constraint is a tolerance threshold to save time. Once Eq. (11) changes less than 10^{-2} from one iteration to the next, the solution is considered converged. This error is the same magnitude of that expected from the simplifications made in Fig. 1 and Fig. 2.

$$\Phi = \sum_{i=1}^{n} (Spectrum_{Simulated} - Spectrum_{Measured})^2 \tag{11}$$

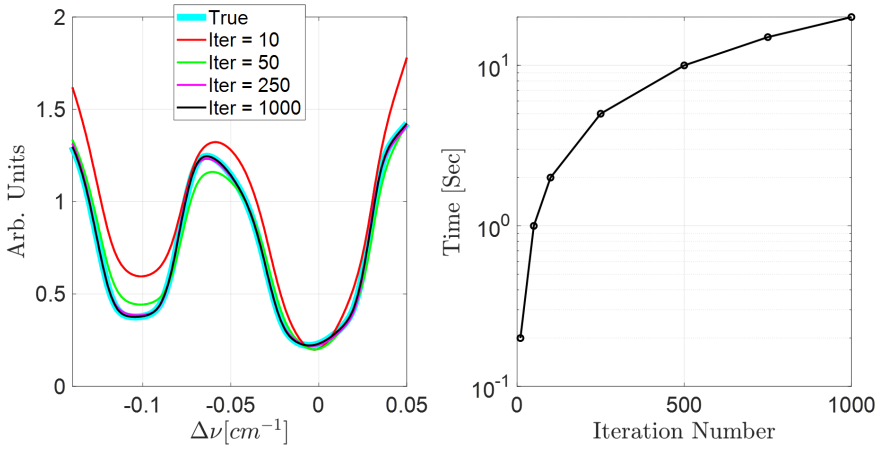

Figure 9. Left: Examples of an iteratively solved solution. Number of iterations noted. Right: Time to generate an iteratively solved spectrum versus the number of iterations used.

The left side of Fig. 9 shows some examples of an iteratively solved solution. The cyan line can be considered as the "true" solution which was found using 10,000 iterations. The colored figure shows that after approximately 250 iterations, a representative solution can be found with diminishing returns. The time needed to compute such a solution can be seen on the right side of Fig. 9. For 250 iterations the time needed to find a solution takes approximately five seconds. Figure 10 backs up these results. Given perfect data (no noise), 250 iterations are more than enough iterations to drive the error in static temperature, velocity, and Mie scattering intensity ratio down below 1%. However, this is not enough for the background scattering intensity ratio. Therefore, 500 iterations must be used as the standard rule. This increases the time it takes to solve to approximately ten seconds. Further work is needed to fully optimize the time required for allowable error bounds.

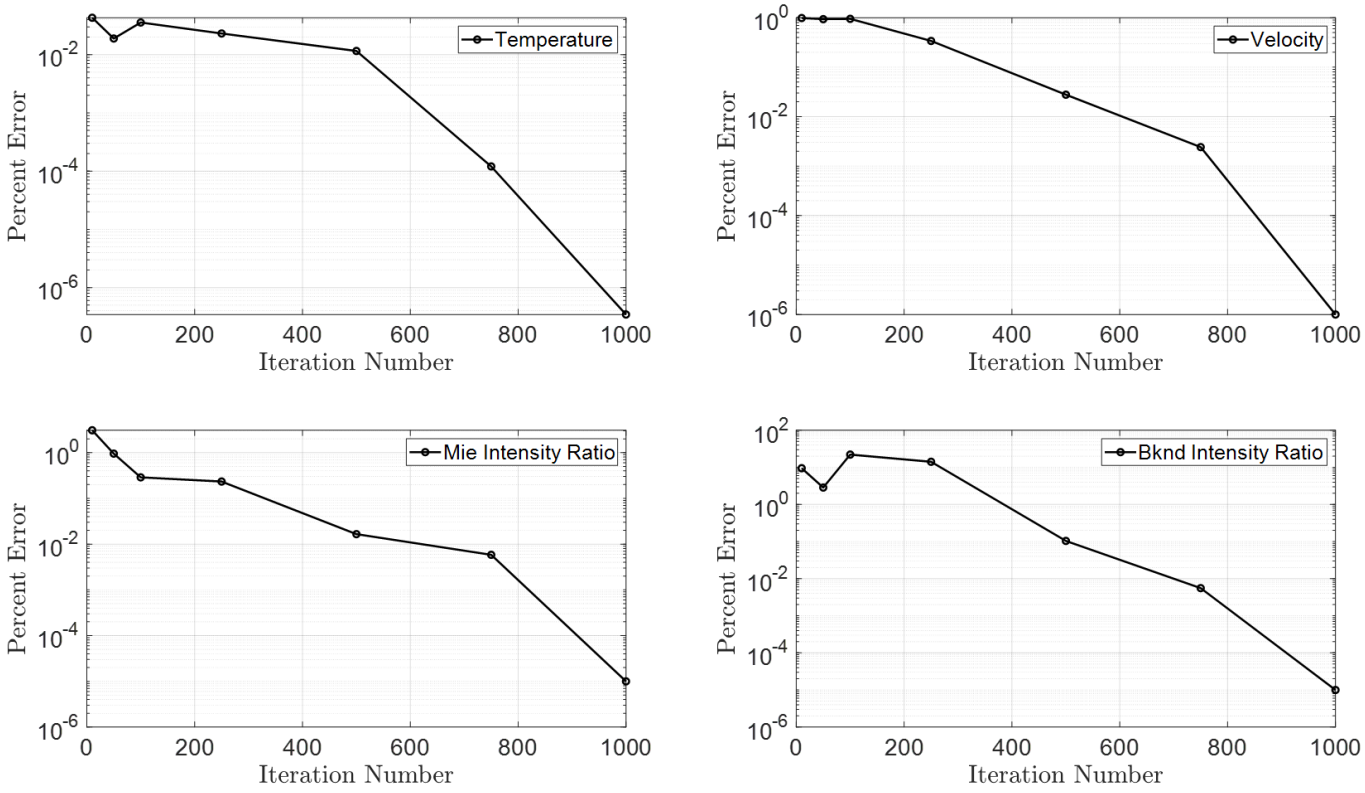

Figure 10. Auto-processing percent error for static temperature, velocity, Mie, and background intensity ratio for noise-free data. The true values were generated using a temperature of 310K, velocity of 135 m/s, background intensity ratio of 0.05, and a Mie intensity ratio of 0.05. These values are important in the next section.

4. Simulation Results and Noisy Uncertainty Results

The results thus far in this paper have been calculated on the assumption of "perfect" data. This means that the signal-to-noise ratio (SNR) (defined in Eq. (12)) is infinite. In other words, no noise is present in the signal. In practice, this is known not to be true. Noise will always exist in the signal. This noise can consist of both random Gaussian noise as well as shot/Poisson noise. This section will show results from applying the automatic process to spectra that contain random Gaussian noise. Shot noise remains of interest but has been left for future work.

$$SNR(dB) = 10log_{10}\left(\frac{P_S}{P_N}\right) \tag{12}$$

The error of the final result from the iteration process varies largely with the SNR. Each variable also has different SNR levels that must be achieved in the measured spectrum to achieve the same kind of uncertainty due to the availability of information in a given signal corresponding to each flow property of interest. To determine these values, Monte Carlo simulations of theoretical spectra were generated over 1028 flow cases with a temperature of 310 K, velocity of 135 m/s, background intensity ratio of 0.05, and Mie intensity ratio of 0.05 for each SNR level. Note that static pressure is not considered. This is due to experimental difficulties and will be addressed in future work.

These Monte Carlo simulations were run at SNR levels of 10, 20, 30, 40, and 50 dB. These generated spectra can be considered as the "measured" spectra and run through the iterative processing code. The effects of using a full spectrum versus a partial spectrum (normal range as defined in Fig. 8) were also investigated (see Fig. 11 for a clear definition). See Fig. 12 for graphical results of the simulations. To achieve an uncertainty of 1% in the velocity measurement, the SNR must be at least 23 dB for a full scan and 25 dB for a partial scan of the spectrum (Fig. 12A). For temperature, the SNR must be at least 25 dB for a full scan and 28 dB for a partial scan (Fig. 12B). For the background intensity ratio, the SNR must be at least 35 dB for a full scan and 38 dB for a partial scan (Fig. 12C). For the Mie intensity ratio, the SNR must be at least 37 dB for a full scan and 41 dB for a partial scan (Fig. 12D).

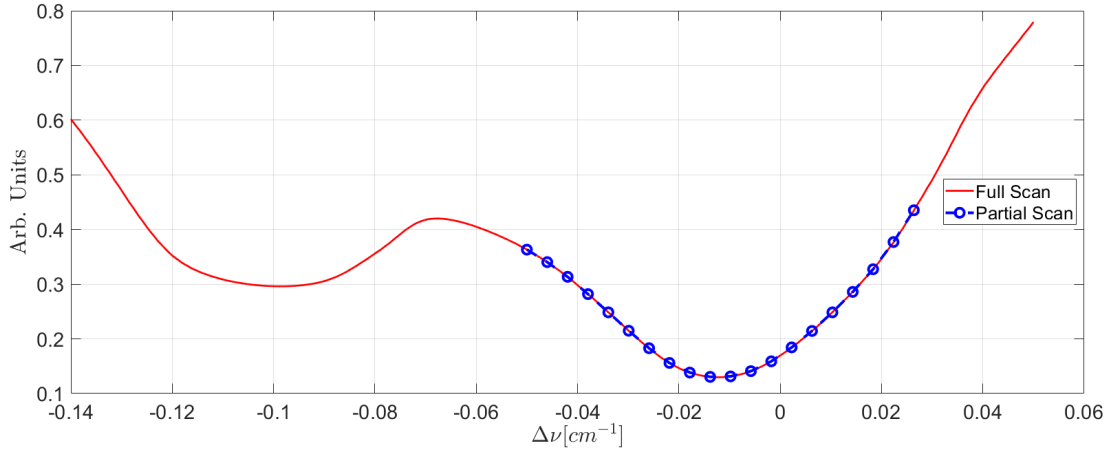

Figure 11. Full-spectrum (red) and partial spectrum (blue).

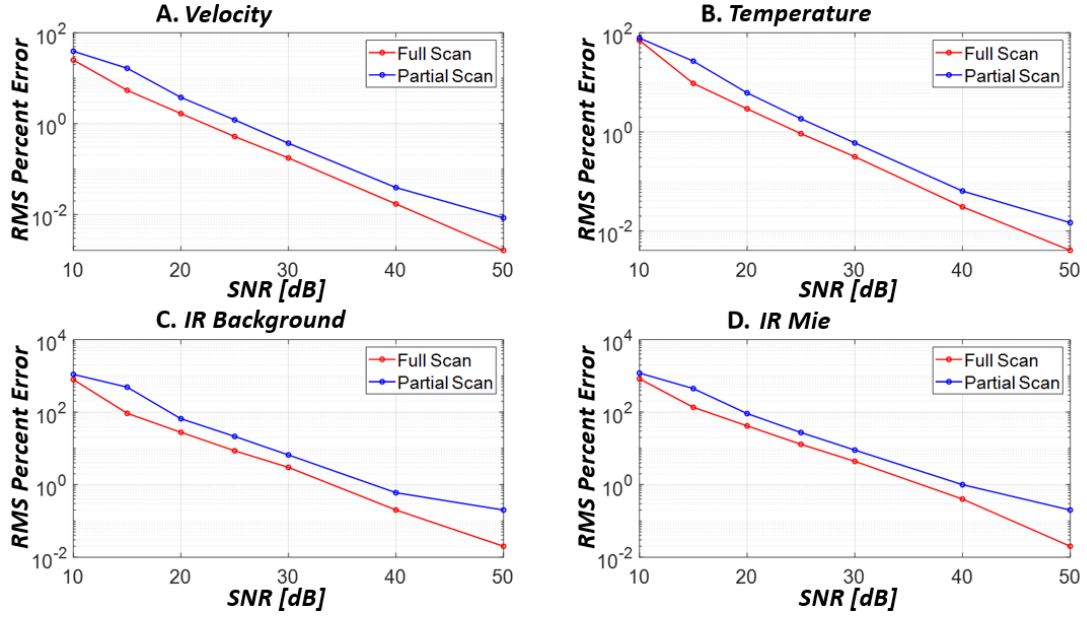

Figure 12. Monte Carlo simulations and relevant conditions at both full-spectrum and partial spectrum scans. Percent error versus SNR.

Figure 13 is a visual representation of simulated data with different SNR levels. The data shown uses a 50x50 grid of data points with no binning (no pixel averaging). Figure 13A represents an SNR of 20 dB, Fig. 13B an SNR of 30 dB, and Fig. 13C an SNR of infinity. The top left contour in each figure represents the axial velocity of a jet. It is clear that even at an SNR level of 20 dB, the velocity profile is easily distinguishable. In contrast, the top right contour in each figure represents the temperature. Below an SNR of approximately 30 dB, the shape of the temperature profile is lost as the uncertainty in its magnitude becomes too high. Both Mie (IR_{Mie}) and background (IR_{Bknd}) scattering intensity ratios were held constant across the planar domain. At an SNR of 20 dB, the uncertainty rises over 50% and the data for these two variables become unusable. Therefore, we would expect that for experimental results to be usable an SNR of at least 25 dB is needed.

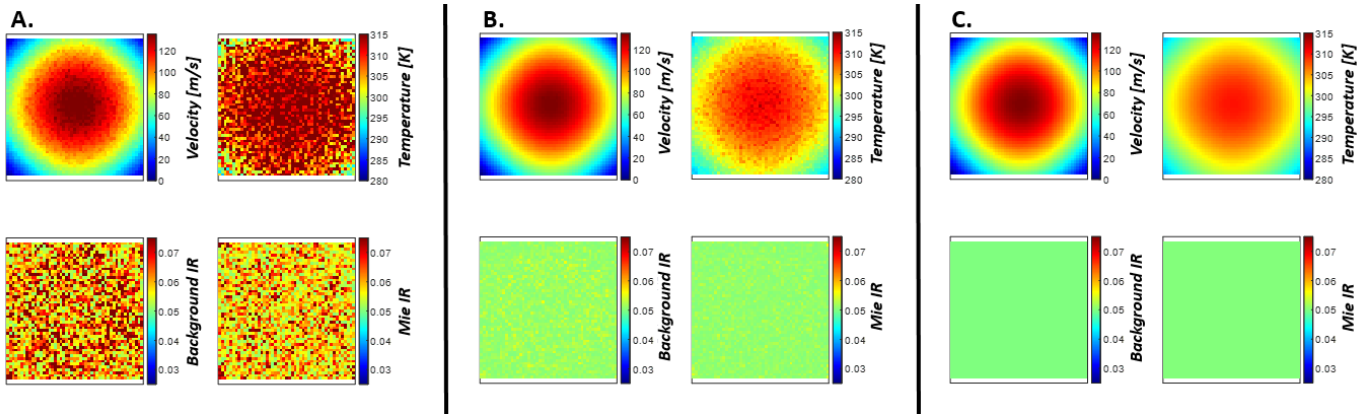

Figure 13. Simulated jet experiment using auto-processing code (colorbars held constant). (A) SNR level of 20. (B) SNR level of 30. (C) Infinite SNR.

5. Experimental Results

To provide experimental validation that this new processing technique works, FRS data was collected using a free jet (Fig. 14C) with approximately the same operating conditions as the simulations. The free jet has a diameter-based Reynolds number of approximately 2.3×10^5. Given the proximity of the cameras, the pixel resolution is about 1mm/pixel. This allowed for approximately 25 pixels across the nozzle exit. A sample raw image from the experiment can be seen in Fig. 14A & 14B. The left side of the image contains large amounts of particles leading to increased Mie scattering (outlined in pink). The jet plume is also outlined in red. Preliminary analysis shows that the SNR in this experiment was close to 20 dB. The low SNR made manual processing very difficult and time consuming. Manual processing methods were incapable of returning temperature results. However, the auto-processing code was able to obtain temperature, velocity, Mie scattering, and background scattering values across the entire plane.

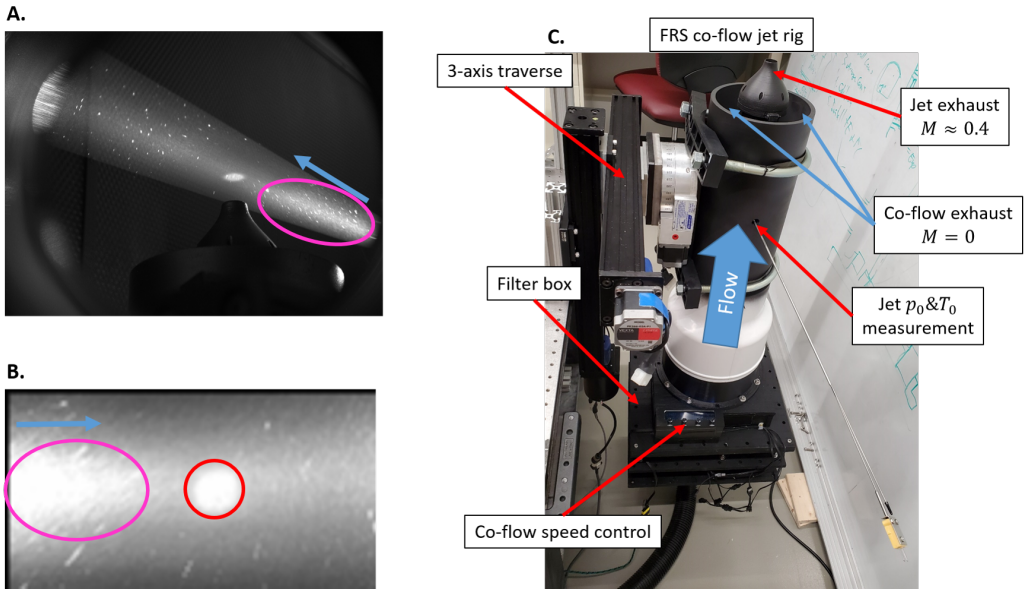

Figure 14. Raw FRS image in the high transmission region of the iodine cell. Jet plume outlined in red. The blue arrow indicates the laser propagation direction. The pink circle shows the area of high particles (more Mie scattering).

The manually iterated result on the far left side of Fig. 15 exhibits approximately 2% error compared to probe data, acceptable for many applications of interest.. However, the time needed for manual iteration, sectioning of the original image, and final processing takes several days. There is also major potential for user input bias. If the user thinks they know what the solution should be they can iterate on scattering values until the "correct" solution is met. This can lead to non-physical values for Mie and Background scattering. For example, a manual iteration with large Mie scattering contributions and small background scattering contributions can look very similar to that which has small Mie scattering contributions and large background scattering contributions. It should also be noted that manual iteration assumes that the Mie and background scattering will be the same over the entire image. The user cannot possibly iterate on these values at every pixel. The automatic processing method can. Given the angle of the cameras and known background, for this experiment the background contribution should be very close to zero. The jet air contained many small dust particles which would lead to higher Mie scattering contributions in the data.

This is exactly what the lower right of Fig. 15 shows. Near the jet, where the number of particles on the left side of the original picture (Fig. 14B) is not affecting the measurement, the background scattering levels are near zero, and the Mie scattering levels are much higher. Again, since this is a time-averaged technique, it makes sense that more particles are seen in the jet plume (more mass flow) compared to outside of the jet plume. The temperature results do not show the jet profile. This is due to the approximately 3% uncertainty ($\pm 10K$) in the temperature results. The probe data shows that the jet profile has a maximum temperature increase of approximately 8 K. Therefore, the profile is lost in the uncertainty. However, the overall temperature magnitude compares well. The velocity results of the auto-processed data match up well with the magnitudes seen in the manually processed data. These velocity results also match well with the probe data with an

approximate error of 2.5%. The variation that can be seen is because the laser frequency resolution was limited due to laser instability and the Mie scattering levels were high. The frequency difference between each data point was large; so, the effect of the noise was high. This caused the fit of our simulated data to the experimental data to be shifted more or less than it should have been. Future experimentation will increase the frequency resolution to get more data points across the spectrum to mitigate this issue. It should be noted that no user inputs were needed to get this result and that it only took approximately one hour for the code to run using six cores on an Intel(R) Xeon(R) CPU E5-1650 at a speed of 3.6 GHz.

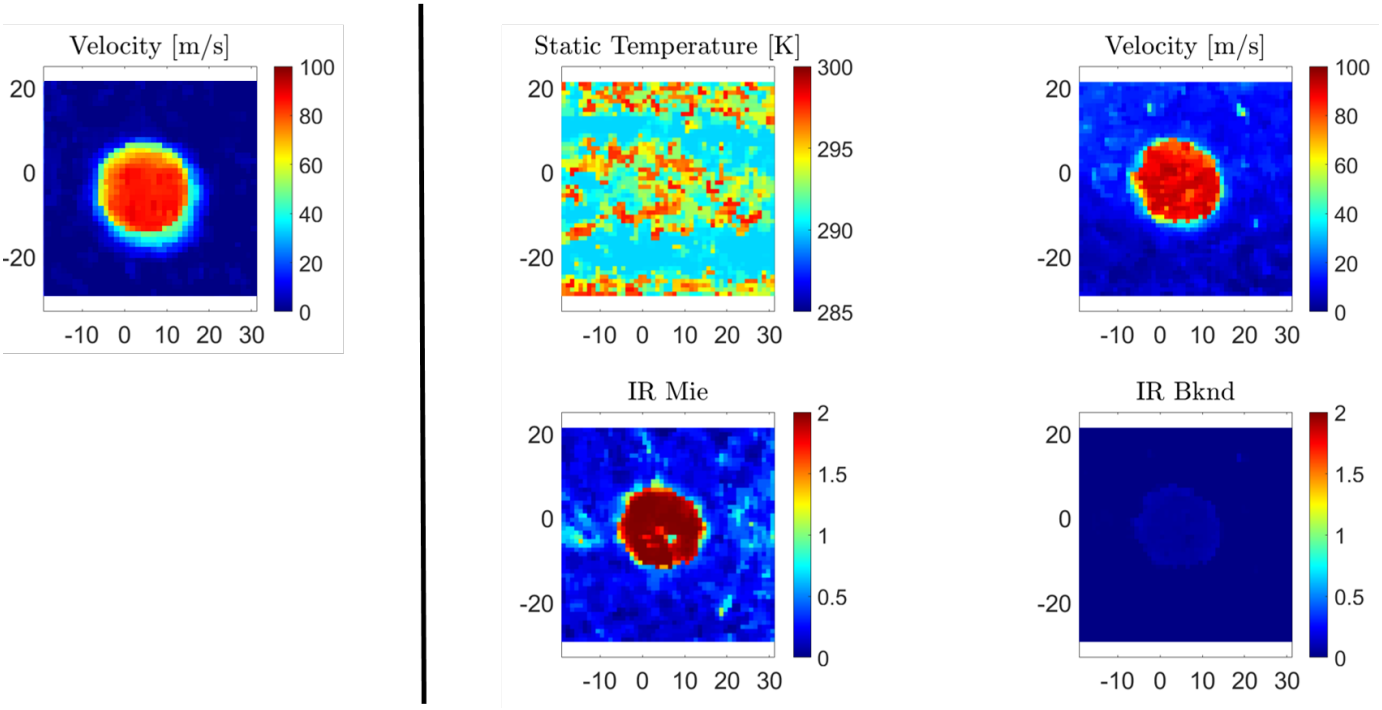

Figure 15. Left: Manually iterated results. Right: Auto-processed results.

6. Conclusions

The post-processing of filtered Rayleigh scattering data for non-intrusive measurements of 3-component velocity, static temperature, background scattering, and Mie scattering is a non-trivial task. It has been shown that an auto-processing scheme that makes use of machine learning (SVSA) and a multi-parameter minimization solver can be used to quickly and accurately determine flow variables. This kind of analysis shows the potential for minimal user input and large time/cost savings in the post-processing of raw FRS data. The new algorithm allows users to quickly and accurately take non-intrusive measurements with the FRS technique and make adjustments day-to-day based on the previous day's data. This was previously impossible due to the amount of manual post-processing needed by the user.

Overall, this paper described the entire FRS modeling technique to generate simulated signals. The equations were presented as well as evidence on what trade-offs were made between accuracy and time. Many of these trade-offs have a compromise where sufficient accuracy and minimal time are required. Perhaps the easiest example of this is the inclusion of the machine learning-based support vector spectrum approximation (SVSA) code that sped up the simulated spectrum generation time while incurring minimal error by a factor of two. These processing methods were first applied to simulated data where different signal-to-noise ratios were compared using Monte Carlo simulations. It was shown that to reach less than 1% error in all variables examined, an SNR level of 40 dB would be needed. This is not practical in an experiment. Therefore, an experiment was completed using a free jet with background and Mie scattering present. These results were compared to manually processed results. The manually processed results consisted of a sensed velocity field (50x50 grid) which took several days to produce. The auto-processed results included sensed velocity, static temperature, Mie intensity ratio, and background intensity ratio and took just an hour to produce. The sensed velocities compared well. The auto-processing method has been shown to have advantages over the manual methods used in the past. It is now clear that the algorithm developed in this work is capable of automatically processing images from experiments with Mie and background scattering contributions with little error.

Future work will be focused on the modeling of noise sources as well as preparation for large planar experiments. Large planar experiments pose a challenge due to the amount of pixels involved. This large number of pixels becomes an issue as the auto-processing time for one pixel may be on the order of a few seconds. Processing millions of pixels on that sort of time scale is not practical, even with parallel processing. Therefore, a multi=pass processing technique is being developed to reduce the iterations needed for each pixel. The mesh size will be allowed to change based on features within the images. This is the last step to produce a fully automatic, efficient, and accurate post-processing tool for filtered Rayleigh scattering.

Nomenclature

c_{int}	internal heat capacity
DGV	Doppler global velocimetry
dB	decibels
FRS	filtered Rayleigh scattering
$FWHM$	full width half maximum
f_u	Euken factor
FRS	filtered Rayleigh scattering
$\hat{i}$	laser propagation vector
$I_{Background}$	background scattering intensity
I_{Mie}	Mie scattering intensity
$I_{Rayleigh}$	Rayleigh scattering intensity

IR_{Bknd}	background scattering intensity ratio
IR_{Mie}	Mie scattering intensity ratio
k	wave vector magnitude
k_b	Boltzmann constant
m	molecular mass
n_o	number density
$\hat{o}$	observation vector
P_S	signal power
P_N	noise power
PIV	particle image velocimetry
R_{int}	internal relaxation number
S_{Bknd}	background scattering spectrum
$S_{Bknd_{Norm}}$	normalized background scattering spectrum
S_{Mie}	Mie scattering spectrum
$S_{Mie_{Norm}}$	normalized Mie spectrum
S_{Ray}	Rayleigh scattering spectrum
$S_{Ray_{Norm}}$	normalized Rayleigh scattering spectrum
S_S	convoluted spectrum
S_{Tot}	Total scattering spectrum
SNR	signal-to-noise ratio
$SVSA$	support vector spectrum approximation
T	temperature
T_{iodine}	iodine transmission spectrum
V	velocity
v_o	gas kinetic velocity
x	non-dimensional modeling parameter for SVSA
y	non-dimensional modeling parameter for SVSA
$\Delta\nu$	wavenumber difference
$\Delta\nu_D$	frequency shift to to Doppler effect
η	dynamic viscosity
η_b	bulk viscosity
θ	scattering angle
λ	wavelength
σ	thermal conductivity
Φ	objective function to minimize error

References

Boguszko, M., & Elliott, G. (2005). Property measurement utilizing atomic/molecular filter-based diagnostics. *Progress in Aerospace Sciences*, *41*(2), 93–142.

Boyda, Byun, G., & Lowe, K. (2018a). Cross-correlation doppler global velocimetry using rayleigh and mie scattering. In *2018 aiaa aerospace sciences meeting* (p. 1766).

Boyda, Byun, G., & Lowe, K. (2018b). Cross-correlation filtered rayleigh scattering (ccfrs). In *19th international symposium on application of laser techniques to fluid mechanics* (pp. 16–19).

Boyda, Byun, G., & Lowe, K. (2019). Investigation of velocity and temperature measurement sensitivities in cross-correlation filtered rayleigh scattering (ccfrs). *Measurement Science and Technology*, *30*(4), 044004.

Boyda, Byun, G., Saltzman, A. J., & Lowe, T. (2020). Influence of mie and geometric scattering contributions on temperature and density measurements in filtered rayleigh scattering. In *Aiaa scitech 2020 forum* (p. 1516).

Cadel, D. R., & Lowe, K. T. (2015). Cross-correlation doppler global velocimetry (cc-dgv). *Optics and Lasers in Engineering*, *71*, 51–61.

Doll, U., Dues, M., Bacci, T., Picchi, A., Stockhausen, G., & Willert, C. (2018). Aero-thermal flow characterization downstream of an ngv cascade by five-hole probe and filtered rayleigh scattering measurements. *Experiments in Fluids*, *59*(10), 1–10.

Doll, U., Stockhausen, G., & Willert, C. (2014). Endoscopic filtered rayleigh scattering for the analysis of ducted gas flows. *Experiments in Fluids*, *55*(3), 1–13.

Doll, U., Stockhausen, G., & Willert, C. (2017). Pressure, temperature, and three-component velocity fields by filtered rayleigh scattering velocimetry. *Optics letters*, *42*(19), 3773–3776.

Fischer, A., Büttner, L., Czarske, J., Eggert, M., & Müller, H. (2008). Measurement uncertainty and temporal resolution of doppler global velocimetry using laser frequency modulation. *Applied optics*, *47*(21), 3941–3953.

Forkey, J. N., Finkelstein, N. D., Lempert, W. R., & Miles, R. B. (1996). Demonstration and characterization of filtered rayleigh scattering for planar velocity measurements. *AIAA journal*, *34*(3), 442–448.

Forkey, J. N., Lempert, W. R., & Miles, R. B. (1997). Corrected and calibrated i 2 absorption model at frequency-doubled nd: Yag laser wavelengths. *Applied optics*, *36*(27), 6729–6738.

Hanson, F., & Morse, T. (1967). Kinetic models for a gas with internal structure. *The Physics of Fluids*, *10*(2), 345–353.

Hanson, F., Morse, T., & Sirovich, L. (1969). Kinetic description of the propagation of plane sound waves in a diatomic gas. *The Physics of Fluids*, *12*(1), 84–95.

Hetlage, M. E., Wu, Y., & Limbach, C. (2019). Feasibility analysis of optically pumped barium vapor for filtered rayleigh scattering at the nd: Yag third harmonic. In *Aiaa aviation 2019 forum* (p. 3382).

Hunt, G. J., Ground, C. R., & Hunt, R. L. (2020). Fast approximations of spectral lineshapes to enable optimization of a filtered rayleigh scattering experiment. *Measurement Science and Technology*, *31*(9), 095203.

Lagarias, J. C., Reeds, J. A., Wright, M. H., & Wright, P. E. (1998). Convergence properties of the nelder–mead simplex method in low dimensions. *SIAM Journal on optimization*, *9*(1), 112–147.

McManus, T. A., Monje, I. T., & Sutton, J. A. (2019). Experimental assessment of the tenti s6 model for combustion-relevant gases and filtered rayleigh scattering applications. *Applied Physics B*, *125*(1), 1–23.

Pan, X. (2003). Coherent rayleigh-brillouin scattering. *Ph. D. Thesis*.

Pan, X., Shneider, M. N., & Miles, R. B. (2004). Coherent rayleigh-brillouin scattering in molecular gases. *Physical Review A*, *69*(3), 033814.

Saltzman, A. J., Boyda, M. T., Lowe, K. T., & Ng, W. (2019). Filtered rayleigh scattering for velocity and temperature measurements of a heated supersonic jet with thermal non-uniformity. In *25th aiaa/ceas aeroacoustics conference* (p. 2677).

Shimizu, H., Lee, S., & She, C.-Y. (1983). High spectral resolution lidar system with atomic blocking filters for measuring atmospheric parameters. *Applied Optics*, *22*(9), 1373–1381.

Tenti, G., Boley, C., & Desai, R. C. (1974). On the kinetic model description of rayleigh–brillouin scattering from molecular gases. *Canadian Journal of Physics*, *52*(4), 285–290.

Witschas, B. (2011). Analytical model for rayleigh–brillouin line shapes in air. *Applied optics*, *50*(3), 267–270.

Yalin, A. P., & Miles, R. B. (1999). Ultraviolet filtered rayleigh scattering temperature measurements with a mercury filter. *Optics letters*, *24*(9), 590–592.